Sampling Design of Synthetic Volume Arrays for Three-Dimensional Microwave Imaging

Wang, Jianping; Yarovoy, Alexander

Important note
To cite this publication, please use the final published version (if applicable).
Please check the document version above.

Sampling Design of Synthetic Volume Arrays for Three-Dimensional Microwave Imaging

Jianping Wang and Alexander Yarovoy, *Fellow, IEEE*

Abstract—In this paper, sampling design of three-dimensional (3-D) synthetic array (i.e., synthetic volume array) for microwave imaging is considered. Generally, the spatial sampling criteria for one- or two-dimensional arrays can be determined based on some narrowband/ultrawideband array theories. However, for 3-D arrays, where antennas are located in a volume instead of over a surface, these existing array theories are no longer straightforwardly applicable. To address the spatial sampling problem of 3-D arrays, we formulate it as a sensor/observation selection problem in this paper. Although some selection approaches exist and are conveniently applicable to small-scale problems, they are either less efficient or provide less optimal results for selection problems with data dimensions of hundreds or even thousands which is typical for microwave imaging. To get the (near-) optimal spatial sampling scheme for 3-D arrays, a greedy algorithm named clustered maximal projection on minimal eigenspace (CMPME) is proposed to select the most informative sampling positions based on some optimality criteria. This algorithm attempts to select the fewest sampling positions by considering an error threshold for the estimated images. Moreover, it has higher computational efficiency compared to the existing approaches. Finally, its effectiveness and selection performances are demonstrated through some imaging examples.

Index Terms—Sensor selection, sampling design, synthetic aperture radar (SAR), three-dimensional (3-D) array, linear inversion.

I. INTRODUCTION

SYNTHETIC aperture radar (SAR) technique provides a compact and cost-efficient solution to a broad range of imaging applications. For short-range 3-D forward-looking imaging, many SAR imaging modalities have been proposed and developed. Among them, Circular SAR (CSAR), Elevation Circular SAR (E-CSAR) [1] and Radial-scanned SAR (RadSAR) are three popular ones. CSAR collects signals by moving an antenna along a circular trajectory on a cross-range plane, thus effectively synthesizing a ring array. It provides very limited down-range resolution for 3-D imaging. By contrast, RadSAR rotates a *linear array* around its center on a plane and forms a planar circular aperture [2], [3]. Compared to CSAR, RadSAR extends the region of k-space spectra of the acquired signals
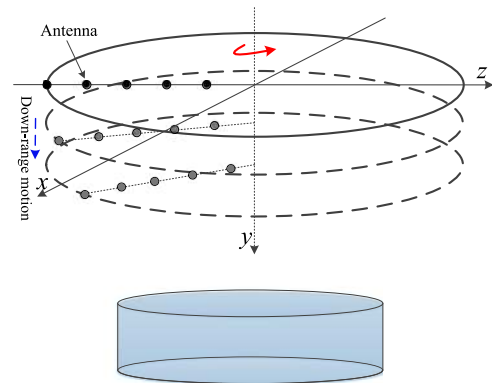
Fig. 1. Illustration of the E-RadSAR formed by taking advantage of synthetic aperture radar technique in the both cross- and down-range directions.

and significantly improves the down-range resolution [4]. On the other hand, on top of CSAR, E-CSAR provides another possibility to get a higher down-range resolution by further exploiting the SAR technique in the down-range direction, which extends the signal acquisition domain from a single circular trajectory to a surface along the down-range direction. Although both RadSAR and E-CSAR increase the down-range resolution, only one antenna is needed for E-CSAR in contrast to a linear array for RadSAR.

Then, an interesting and meaningful question arises: How can we combine both the RadSAR and the forward motion in the down-range direction so as to reduce the number of antennas needed compared to the traditional RadSAR? To answer this question, we propose a new SAR modality, named as *Elevation-RadSAR* (E-RadSAR, see Fig. 1). This new SAR modality is very attractive for cost-tight and/or space-limited applications, such as the cardiac catheter used for intravascular imaging [5] and ground prediction radar (GPR) system for tunnel boring machine (TBM) [6]. The latter is actually our motivation of this study, where the GPR antennas mounted on the cutter-head of a TBM acquire signals with its rotation but the available space for GPR antennas is extremely limited due to mechanical constraints. So reducing the number of antennas needed is very significant for TBM design.

Since E-RadSAR exploits the SAR technique in both cross- and down-range directions, it takes spatial samples of scattered electromagnetic fields in a volume domain and effectively synthesizes a volume array. Thus, designing a proper 3-D sampling scheme is crucial for E-RadSAR to reduce antennas needed. However, the unique 3-D sampling scheme, which is

substantially distinct from that of conventional arrays, makes no longer applicable traditional array analysis and design methods developed based on the projection-slice theorem [7]. On the other hand, the Number of Degrees of Freedom (NDF) of scattered field related to an observation domain provides a general insight for sampling representation, which closely relates to the spectra of scattering/radiation operators [8]. This concept has been used to reduce sampling data over a planar observation domain by investigating the singular spectrum of the scattering operator [9]. In [10], the impact of spatial diversity on the singular spectrum of the radiation operator was analyzed for an extended two-dimensional observation domain, but no practical sampling scheme was given [10]. Beyond spatial diversity, for short-range applications, ultrawideband signals not only provide high-range resolution but also give the potential for sparse spatial sampling (i.e. sparse array) [11]. In addition, the orientations of antennas of E-RadSAR constantly change with its rotation, thus diversifying the polarizations of acquired signals within the aperture. Therefore, how to properly account for the effects of bandwidth and polarization on the signal acquisition of E-RadSAR makes the sampling problem even complicated.

To tackle the sampling problem of E-RadSAR, we formulate it as a sensor/observation selection problem in this paper. Specifically, we assume the antennas can take measurements within a volume over some grids which form a candidate set of spatial samples. Then for a synthetic volume array, sampling design is converted to select a subset of antennas and their spatial sampling positions. In a more general sense, it becomes a subset selection problem. The subset selection has been used for magnetic resonance imaging observation selection [12]–[15], sensor selection/management [16]–[22], array optimization for remote image formation [23], [24], sampling design for detection problem [25], etc. Many selection methods have been developed based on heuristic optimization algorithms (e.g., genetic algorithm, particle swarm), convex optimization, and greedy search approaches with various selection criteria.

However, most of these selection methods are dedicated to sensor selection where one sensor takes one measurement and thus contributes to one row of the observation matrix. In practice, in an imaging system, one antenna usually acquires multiple measurements at a position by utilizing frequency and/or polarization diversities. Therefore, selecting one sensor affects a number of rows in the observation matrix. This was considered as the vector measurement selection in [17] and tackled by relaxing the boolean representation of the selection problem onto a convex set. Then a convex optimization method was used to search a near-optimal solution. Due to the relaxation, the searched solution can be only guaranteed within a certain distance from the truly optimal one. In [23], Sharif *et al.* explored the similar problem and provided a greedy method, i.e., Clustered Sequential Backward Selection (CSBS) to optimize the imaging array for remote sensing. As an inversion of a large matrix is needed for each selection, CSBS becomes less efficient or intractable when the number of candidate sensors/observations is very large. Actually, for imaging applications, the measurements are typically of hundreds or even thousands. In [22] and

[24], the traditional frame potential (FP, a performance metric of orthogonality) based greedy algorithm has been extended to optimize the topology of a radar network for localization and GPR spatial sampling for inversion, where each sensor collects a vector measurement over time or space. Although the extended frame-potential based algorithms are very efficient, their performances are degraded for observation vectors with unequal norms. Moreover, a Maximum Projection on Minimum Eigenspace (MPME) method greedily examines the incremental impact of a new observation vector on the singular value spectrum of the observation matrix formed by existing ones, which accounts for both orthogonalities among observation vectors and their norms. MPME is computationally efficient but it only considers the "single sensor single measurement" case.

In this paper, we further develop the MPME [19] to select sensors with vector (or cluster) measurements, named as clustered MPME (CMPME). In the proposed CMPME, at each time the clustered subset of observation vectors is selected by considering not only the extra information brought by the corresponding measurements/observations as a cluster relative to the existing ones but also the correlations among them within the cluster so as to get overall optimal/near-optimal selections. The proposed method is applicable to any linearized measurement scheme. In the paper, we apply it to the Born-based imaging.

The rest of the paper is organized as follows. In Section II, a linear inversion model for microwave imaging is introduced based on the Born approximation, and the related sensor/sample selection problem is formulated. Then the proposed CMPME algorithm and its efficient implementation are presented in Section III. After that, Section IV shows some imaging examples to demonstrate the performance of CMPME. Finally, conclusions are drawn in Section V.

II. Signal Model

A. Linear Inversion Problem

Assuming the Born approximation is applicable for the electromagnetic (EM) field scattering process from objects, then the scattered field can be linearly represented as [26]

$$
\begin{aligned}
E^s_{\alpha\beta}(\mathbf{x}^t, \mathbf{x}^r, \omega) &= \int_V G_{\alpha\ell}(\mathbf{x}^r; \mathbf{x}^s, \omega)\, \chi(\mathbf{x}^s) \\
&\quad G_{\ell\beta}(\mathbf{x}^s; \mathbf{x}^t, \omega)\, w(\omega)\, \mathrm{d}V \\
&= \int_V D_{\alpha\beta}(\mathbf{x}^t, \mathbf{x}^r; \mathbf{x}^s, \omega)\, \chi(\mathbf{x}^s)\, w(\omega)\, \mathrm{d}V
\end{aligned}
\tag{1}
$$

where ω is the angular frequency, $w(\omega)$ is the spectrum of the radiated wavelet, subscripts α and β indicate the polarizations of receiving and transmitting antennas, $\ell \in \{1, 2, 3\}$ represents three orthogonal components of the electric field, and the Einstein summation convention is used to repeated subscripts. $G_{\ell\beta}(\mathbf{x}^s; \mathbf{x}^t, \omega)$ and $G_{\alpha\ell}(\mathbf{x}^r; \mathbf{x}^s, \omega)$ are Green's functions representing the propagation processes of the EM wave from a β-polarized transmitting antenna at $\mathbf{x}^t$ to a scatterer at $\mathbf{x}^s$ and from the scatterer at $\mathbf{x}^s$ to a α-polarized receiving antenna at

$\mathbf{x}^r$, respectively. $\chi(\mathbf{x}^s)$ denotes the EM scattering properties of a scatterer at $\mathbf{x}^s$. $D_{\alpha\beta}$ is defined as the inner product of $G_{\alpha\ell}$ and $G_{\ell\beta}$, which is given by

$$D_{\alpha\beta} = G_{\alpha\ell}\left(\mathbf{x}^r;\mathbf{x}^s,\omega\right)G_{\ell\beta}\left(\mathbf{x}^s;\mathbf{x}^t,\omega\right) \tag{2}$$

For numerical processing, (1) can be written in the discrete form as

$$E^s_{\alpha\beta}\left(\mathbf{x}^t,\mathbf{x}^r,\omega\right) = w\left(\omega\right)\Delta V \sum_{i=1}^{m} D_{\alpha\beta}\left(\mathbf{x}^t,\mathbf{x}^r;\mathbf{x}^s_i,\omega\right)\chi\left(\mathbf{x}^s_i\right) \tag{3}$$

where m is the number of discrete cells in the imaging domain, and ΔV is the volume of each cell. Considering all the measurements acquired at p discrete frequencies within the operational bandwidth by L transceivers/transmitter-receiver pairs, one can obtain

$$\mathbf{s} = \mathbf{D}\cdot\mathbf{x} \tag{4}$$

where

$$\mathbf{s} = \text{vec}\left(\left[\mathbf{s}_1,\ \mathbf{s}_2,\ \ldots,\ \mathbf{s}_L\right]\right) \tag{5}$$

$$\mathbf{s}_l = \left[E^s_{\alpha_l\beta_l}(\mathbf{x}^r_l,\mathbf{x}^t_l,\omega_1), E^s_{\alpha_l\beta_l}(\mathbf{x}^r_l,\mathbf{x}^t_l,\omega_2),\right.$$
$$\left.\ldots, E^s_{\alpha_l\beta_l}(\mathbf{x}^r_l,\mathbf{x}^t_l,\omega_p)\right]^{\mathsf{T}} \tag{6}$$

$$\mathbf{D} = \left[\mathbf{D}_1,\mathbf{D}_2,\ldots,\mathbf{D}_L\right]^{\mathsf{T}} \tag{7}$$

$$\mathbf{D}_l = \left[\mathbf{D}^{(1)}_l,\ \mathbf{D}^{(2)}_l,\ \ldots,\ \mathbf{D}^{(p)}_l\right] \tag{8}$$

$$\mathbf{D}^{(n)}_l = \left[D_{\alpha_l\beta_l}(\mathbf{x}^r_l,\mathbf{x}^t_l;\mathbf{x}^s_1,\omega_n), D_{\alpha_l\beta_l}(\mathbf{x}^r_l,\mathbf{x}^t_l;\mathbf{x}^s_2,\omega_n),\right.$$
$$\left.\ldots, D_{\alpha_l\beta_l}(\mathbf{x}^r_l,\mathbf{x}^t_l;\mathbf{x}^s_m,\omega_n)\right]^{\mathsf{T}} \tag{9}$$

$$\mathbf{x} = \left[\chi(\mathbf{x}^s_1),\ \chi(\mathbf{x}^s_2),\ \ldots,\ \chi(\mathbf{x}^s_m)\right]^{\mathsf{T}} \tag{10}$$

and $l = 1, 2, \ldots, L$, $n = 1, 2, \ldots, p$. In the above equations, $\text{vec}(\cdot)$ stacks the columns of an $m \times n$ matrix as an $mn \times 1$ column vector, and $(\cdot)^{\mathsf{T}}$ denotes the transpose of a matrix. The subscripts α_l and β_l indicate the polarizations of the l-th transceiver/transmitter-receiver pairs. Moreover, the term $w(\omega)\Delta V$ is suppressed for simplification in (4). According to (4)–(10), one can see that the measurement vector $\mathbf{s} \in C^{L\cdot p}$, and the vector of scattering coefficients $\mathbf{x} \in C^m$. $\mathbf{D} \in C^{(L\cdot p)\times m}$ is the sensing matrix and each row is an observation vector related to a measurement. Theoretically, to accurately reconstruct contrast functions of targets, a great number of measurements should be collected by transceivers at various positions, which is usually determined by the Nyquist criteria and $L\cdot p \gg m$.

However, due to some practical constraints (i.e., cost, space and bandwidth) of the imaging systems, only a small number of measurements of scattered EM fields can be acquired. The measured signals can be represented as

$$\mathbf{y} = \mathbf{H}\mathbf{s} = \mathbf{A}\mathbf{x} + \mathbf{n} \tag{11}$$

where $\mathbf{H} \in R^{M\times(L\cdot p)}$ is the selection matrix whose rows are the standard bases $\mathbf{e}^{\mathsf{T}}_{s_i}$s (here the subscript s_i indicates the index of the non-zeros entry in a standard basis), $i = \{1, 2, \ldots, M\}$, and M is the number of the selected rows of $\mathbf{D}$. The M selected rows

from $\mathbf{D}$ indexed by $\{s_1, s_2, \cdots, s_M\}$ form the observation matrix $\mathbf{A} \in C^{M\times m}$. $\mathbf{n} \in C^M$ is the measurement errors and noise of Gaussian distribution with zero mean and $\sigma^2\mathbf{I}$ the variance. Assuming $M \geq m$ measurements are acquired by the imaging system, the least squares estimate of the contrast function is given by

$$\hat{\mathbf{x}} = \mathbf{A}^{\dagger}\mathbf{y} = (\mathbf{A}^H\mathbf{A})^{-1}\mathbf{A}^H\mathbf{y} \tag{12}$$

where $(\cdot)^H$ represents the conjugate transpose of a matrix, and $\mathbf{A}^{\dagger} = (\mathbf{A}^H\mathbf{A})^{-1}\mathbf{A}^H$ is the pseudo-inverse of $\mathbf{A}$. The accuracy of the reconstructed $\hat{\mathbf{x}}$ with the observation matrix $\mathbf{A}$ can be examined via the metrics:

- Mean square error (MSE)

$$\text{MSE}(\hat{\mathbf{x}}) = E[\|\hat{\mathbf{x}} - \mathbf{x}\|^2_2]$$
$$= \sigma^2\text{tr}(\mathbf{\Gamma}^{-1}) = \sigma^2\sum_{i=1}^{m}\frac{1}{\lambda_i} = \sigma^2\|\mathbf{A}^{\dagger}\|^2_F \tag{13}$$

where $\mathbf{\Gamma} = \mathbf{A}^H\mathbf{A}$, and $\lambda_1 \geq \lambda_2 \geq \cdots \geq \lambda_m$ are its non-increasing eigenvalues. $\text{tr}(\cdot)$ and $\|\cdot\|_F$ denote trace and the Frobenius norm, respectively.

- Worst case error variance (WCEV)

$$\text{WCEV}(\hat{\mathbf{x}}) = \lambda_{\max}(\sigma^2\mathbf{\Gamma}^{-1}) = \sigma^2\frac{1}{\lambda_m} = \sigma^2\|\mathbf{A}^{\dagger}\|^2_2 \tag{14}$$

where $\lambda_{\max}(\cdot)$ represents the maximum eigenvalue of a matrix and $\|\cdot\|_2$ is the 2-norm operator.

From (13) and (14), One can see that MSE and WCEV are closely related as $\text{MSE}(\hat{\mathbf{x}}) \leq m\cdot\text{WCEV}(\hat{\mathbf{x}})$. So minimizing the WCEV equivalently reduces the upper bound of MSE. Besides, the condition number of the observation matrix $\mathbf{A}$ is often used to indicate the sensitivity of $\hat{\mathbf{x}}$ with respect to the error of the measurement data and defined by

$$\text{CondNo}(\mathbf{A}) = \sqrt{\lambda_1/\lambda_m} \tag{15}$$

As $\lambda_1 \geq \lambda_m$, the condition number of $\mathbf{A}$ is not less than one. If the condition number is small, then small changes in the measurement data will result in small errors in the estimation of $\mathbf{x}$. Otherwise, small changes in the measurement data will lead to large errors in the estimation of $\mathbf{x}$.

According to (13)–(15), MSE, WCEV and the condition number are all dependent on the eigenvalues of the matrix $\mathbf{\Gamma}$, thus fully depending on the observation matrix $\mathbf{A}$. As indicated in (11), $\mathbf{A}$ is a function of antenna positions, polarizations and frequencies. So its recovery performance can be optimized by properly designing antenna positions, polarizations and frequencies used in an imaging system. Hence, the above linear system formulation provides a unified framework to explore spatial-, polarization- and frequency-diversities for microwave imaging system design.

B. Problem Statement

Here we assume the imaging system works at a certain bandwidth and the antenna polarizations are fixed (but could be

different) at each position. Only spatial sampling of synthetic volume array, i.e., E-RadSAR, for 3-D imaging is considered.

In principle, the 3-D spatial sampling problem of E-RadSAR can be handled by transforming to a sensor/observation selection problem. As E-RadSAR exploits the rotation of a linear array in cross-range and its forward motion in down-range direction, the related sensor/observation selection procedure is naturally divided into two steps: (1) selecting a specific number of sensors (antennas); (2) determining the spatial sampling strategy for each antenna. On the other hand, the selection procedure can also be organized as: (1) first selecting (near-)optimal sampling configuration for a volume array; (2) then determining antenna positions to implement such configuration. These two selection schemes determine the antenna positions and spatial samples in different orders and could lead to different selection results. The first selection scheme implicitly confines the number of antennas used by the imaging system while the second one could get better spatial sampling configuration but more antennas are probably needed. In practice, the selection scheme can be decided based on the resource constraints of imaging systems.

However, as the radar system operates at a certain bandwidth, multiple measurements can be acquired at different frequencies in each spatial sampling position. Thus, in either selection scheme above, a vector-measurement subset selection problem is involved. Actually, besides the E-RadSAR, sampling designs for general microwave imaging systems can be formulated as a vector-measurement selection problem. For convenience of description, we denote the set of the N candidate positions as $\mathcal{N} = \{1, 2, \ldots, N\}$ and the set of M selected positions $\mathcal{S} = \{s_1, s_2, \ldots, s_M\}$. The initial sensing matrix $\tilde{\mathbf{A}} = [\mathbf{\Phi}_1, \mathbf{\Phi}_2, \ldots, \mathbf{\Phi}_N]^\mathsf{T} \in \mathbb{C}^{(N \cdot Q) \times m}$, where $\mathbf{\Phi}_i^\mathsf{T} \in C^{Q \times m}$ is a submatrix formed by Q observation vectors associated with the i-th candidate position. Then, the sensor/observation placement problem with vector measurement can be formally expressed as follows.

Problem 1: Giving the initial sensing matrix $\tilde{\mathbf{A}} = [\mathbf{\Phi}_1, \mathbf{\Phi}_2, \ldots, \mathbf{\Phi}_N]^\mathsf{T} \in C^{(N \cdot Q) \times m}$, where $\mathbf{\Phi}_i^\mathsf{T} \in C^{Q \times m}$, select M submatrices of $\tilde{\mathbf{A}}$ indexed with $[s_1, s_2, \ldots, s_M]$ in $\mathcal{N}$ to construct an observation matrix $\mathbf{A} = [\mathbf{\Phi}_{s_1}, \mathbf{\Phi}_{s_2}, \ldots, \mathbf{\Phi}_{s_M}]^\mathsf{T} \in C^{(M \cdot Q) \times m}$, such that the estimation error satisfies certain requirements and the number of selected submatrices is minimized.

It can be found that the difference of *Problem 1* from the one addressed in [19] is that submatrices instead of individual rows are selected here. By consecutively tackling the *Problem 1* for antenna and their spatial observation selection, the sampling strategy of the E-RadSAR can be determined.

III. CLUSTERED MAXIMAL PROJECTION ON MINIMAL EIGENSPACE

In this section, the Clustered Maximal Project on Minimal Eigenspace (CMPME) is proposed to address the aforementioned vector measurement selection problem. Moreover, an iterative implementation scheme is suggested to accelerate the CMPME algorithm.

A. CMPME

CMPME further develops the MPME algorithm for selecting sensors/observations with vector measurement. Similar to MPME, the objective of the CMPME algorithm is in essence to select the minimum number of sensors such that their observation vectors form an observation matrix $\mathbf{A}$ with m significant singular values. The basic idea of the CMPME algorithm is to select the sensor that brings the most information complementary to that of the existing ones at a time.

Assume an observation matrix $\mathbf{A}_{k-1} \in C^{(k-1)Q \times m}$ is formed by the observation vectors related to the first $k-1$ selected sensors with Q measurements for each. Its singular value decomposition (SVD) can be denoted as $\mathbf{A}_{k-1} = \mathbf{U}\mathbf{\Sigma}\mathbf{V}^H$, where $\mathbf{U} \in C^{(k-1)Q \times (k-1)Q}$ and $\mathbf{V} \in C^{m \times m}$ are left and right unitary matrices and $\mathbf{\Sigma} \in R^{(k-1)Q \times m}$ is a diagonal matrix with nonnegative real numbers in the diagonal. The column vectors of $\mathbf{U}$ and $\mathbf{V}$ span the data space and the object's space, respectively. To get an observation matrix for unambiguous reconstruction of the object, the most efficient observations are those that gradually expand the dimension of the data space to be close or equal to that of the object's space. So it is better to select as the kth sensor the one that brings the most complementary information with respect to the existing $k-1$ ones.

To determine the kth optimal sensor to be selected, the complementary information brought by a new sensor can be evaluated by checking the effects of its associated observation vectors on the singular value system of the observation matrix $\mathbf{A}_{k-1}$ (equivalently, the effects on the eigenvalue system of the "dual observation matrix" $\mathbf{A}_{k-1}^H \mathbf{A}_{k-1}$). Specifically, when the number of observation vectors related to the $k-1$ sensors is less than that of the unknowns in the beginning, i.e., $(k-1)Q \leq m$, the Q observation vectors associated with a new sensor that have the largest component (i.e., projection) in the null space of the observation matrix $\mathbf{A}_{k-1}$ expand the dimension of the data space and contribute the most complementary information. Thus, the corresponding sensor should be the kth selection. Inserting the Q newly selected observation vectors into $\mathbf{A}_{k-1}$, a new observation matrix $\mathbf{A}_k$ is constructed with the row dimension increased by Q. Accordingly, the number of significant singular values of $\mathbf{A}_k$ also increases compared to $\mathbf{A}_{k-1}$. When $(k-1)Q > m$ and all the singular values are positive, the rows of $\mathbf{A}_{k-1}$ form an over-complete set of bases for its row space. To reduce the estimation errors of the solution [see (13) and (14)], the observation vectors of a new sensor should increase the minimum singular value of the updated observation matrix $\mathbf{A}_k$ (equivalently, to increase the minimum eigenvalue of the "dual observation matrix" $\mathbf{A}_k^H \mathbf{A}_k$ [19]). Then the kth selected sensor is the one whose observation vectors have the largest projection onto the *minimum eigenspace* which is spanned by the eigenvector(s) associated with the minimum eigenvalue(s) of $\mathbf{A}_{k-1}^H \mathbf{A}_{k-1}$.

However, for vector measurement selection, selecting one sensor results in choosing Q observation vectors at a time, which is distinct from the traditional "single sensor single measurement" case. By examining the projection of the Q newly selected vectors onto the minimum eigenspace of $\mathbf{A}_{k-1}^H \mathbf{A}_{k-1}$,

we only consider their "orthogonalities" with respect to the existing row vectors of $\mathbf{A}_{k-1}$. However, to guarantee that each measurement brings the most complementary information relative to the rest, to what extent the Q observation vectors of a sensor for the kth selection are mutually orthogonal should be evaluated as well. Specifically, when the observation vectors associated with two sensors have equal projections onto the minimum eigenspace of $\mathbf{A}_{k-1}^H \mathbf{A}_{k-1}$, the one whose associated observation vectors are more mutually orthogonal is preferred. This can be derived as follows. If we allow the Q observation vectors associated with a sensor to be selected individually, each time the observation vector that has the largest projection onto the minimum eigenspace of $\mathbf{A}_{k-1}^H \mathbf{A}_{k-1}$ is picked. If the number of the rows of $\mathbf{A}_{k-1}$ is smaller than m, the minimum eigenspace of $\mathbf{A}_{k-1}^H \mathbf{A}_{k-1}$ is the null space of $\mathbf{A}_{k-1}$. So the newly selected observation vector is always to the largest extent "orthogonal" to the existing rows in the observation matrix. This is also true for the last Q selected observation vectors. However, now we have to select Q vectors as a group at a time. So it is natural that the Q newly selected observation vectors should not only have the largest projection onto the minimum eigenspace of $\mathbf{A}_{k-1}^H \mathbf{A}_{k-1}$ but also be to the largest extent mutually "orthogonal".

To quantitatively assess the orthogonality among the Q observation vectors of a sensor, the inner products among their corresponding normalized vectors are conducted. As we prefer the sensors whose observation vectors are more close to orthogonal, the inner products among them should be more close to zeros. By considering both the projection of the new observation vectors onto the minimum eigenspace and their orthogonality, the optimal sensor can be selected by maximizing the cost function

$$\text{Cost}(\mathbf{\Phi}_{s_k}) = \|\mathbf{P}_{k-1}\mathbf{\Phi}_{s_k}\|_F^2 - \eta \left(\sum_{i,j=1}^{Q} |\langle \tilde{\varphi}_i, \tilde{\varphi}_j \rangle|^2 \right) \quad (16)$$

where $\mathbf{\Phi}_{s_k}$ is the small matrix formed by the Q observation vectors $\varphi_i, i = 1, 2, \ldots, Q$, and $\tilde{\varphi}_i$ is the normalized vector of φ_i. $\mathbf{P}_{k-1}$ is the projection operator onto the minimum eigenspace of $\mathbf{A}_{k-1}^H \mathbf{A}_{k-1}$. $\langle \cdot \rangle$ and $|\cdot|$ are the inner product and the absolute value, respectively. η is a constant parameter that controls the importance of the orthogonality among the new observation vectors, which should be chosen based on the correlations among the observation vectors for specific scenarios. Actually, the second term in (16) is related to the inverse frame potential of the new sensor. Therefore, the cost function in (16) is, to some extent, a combination of the projection and the frame potential.

The projection operator at each step can be obtained in a similar way as in [19]. When $(k-1)Q \leq m$, the minimum eigenspace of $\mathbf{A}_{k-1}^H \mathbf{A}_{k-1}$ is the null space of $\mathbf{A}_{k-1}$. Then the projection matrix $\mathbf{P}_{k-1}$ onto the minimum eigenspace of $\mathbf{A}_{k-1}^H \mathbf{A}_{k-1}$ can be given by

$$\mathbf{P}_{k-1} = \mathbf{I}_{m \times m} - \mathbf{R}_{k-1}\mathbf{R}_{k-1}^H \quad (17)$$

where $\mathbf{I}_{m \times m}$ is the $m \times m$ identity matrix and $\mathbf{R}_{k-1} = \text{orth}(\mathbf{A}_{k-1}^H)$ whose column vectors are obtained from the Gram-Schmidt Orthonormalization of all the column vectors of $\mathbf{A}_{k-1}^H$ [27]. When $(k-1)Q > m$, the projection matrix $\mathbf{P}_{k-1}$ is

---

Algorithm 1: Clustered Maximal Projection on Minimum Eigenspace.

1: **Input:** $\tilde{\mathbf{A}} = \{\mathbf{\Phi}_1, \mathbf{\Phi}_2, \ldots, \mathbf{\Phi}_N\}^\mathsf{T} \in C^{(N \cdot Q) \times m}$, where $\mathbf{\Phi}_i^\mathsf{T} \in C^{Q \times m}$
2: **Output:** $\mathbf{A} \in C^{(M \cdot Q) \times m}, \mathcal{S}, M$
3: 1) **Initialization:** $\mathcal{N} = \{1, 2, \ldots, N\}, \mathcal{S} = \emptyset$.
4: 2) **Determine the first** $n = \lceil \frac{m}{Q} \rceil$ **sampling positions:**
5: (a) Set $\mathbf{A}_0 = [], \mathbf{P}_0 = \mathbf{I}_{n \times n}$ and $k = 1$.
6: (b) $\hat{s}_k = \arg \max_{i \in \mathcal{N} \setminus \mathcal{S}} \text{Cost}(\mathbf{\Phi}_i)$.
7: (c) Update: $\mathcal{S} = \mathcal{S} \cup \{\hat{s}_k\}, \mathbf{A}_k = [\mathbf{A}_{k-1}^\mathsf{T} \quad \mathbf{\Phi}_{\hat{s}_k}]^\mathsf{T}$, $\mathbf{R}_k = \text{orth}(\mathbf{A}_k^H), \mathbf{P}_k = \mathbf{I}_{m \times m} - \mathbf{R}_k\mathbf{R}_k^H$.
8: (d) Set $k = k + 1$ and repeat step (b-c) until $k = n$.
9: 3) **Determine the remaining sampling positions:**
10: (a) $\hat{s}_k = \arg \max_{i \in \mathcal{N} \setminus \mathcal{S}} \text{Cost}(\mathbf{\Phi}_i)$.
11: (b) Update: $\mathcal{S} = \mathcal{S} \cup \{\hat{s}_k\}, \mathbf{A}_k = [\mathbf{A}_{k-1}^\mathsf{T} \quad \mathbf{\Phi}_{\hat{s}_k}]^\mathsf{T}$, $\mathbf{A}_k^H = \mathbf{U}^{(k)}\mathbf{\Sigma}^{(k)}(\mathbf{V}^{(k)})^H, \mathbf{P}_k = \mathbf{U}_{m \times \mu_m}^{(k)}(\mathbf{U}_{m \times \mu_m}^{(k)})^H$.
12: (c) If $\lambda_m^{(k)} > \gamma$ return $\mathcal{S}, M = k$ and $\mathbf{A} = \mathbf{A}_k$; else set $k = k + 1$ and repeat step (a-b).

---

expressed as

$$\mathbf{P}_{k-1} = \mathbf{U}_{m \times \mu_m}^{(k-1)}(\mathbf{U}_{m \times \mu_m}^{(k-1)})^H \quad (18)$$

where $\mathbf{U}_{m \times \mu_m}^{(k-1)} = [\mathbf{u}_{m-\mu_m+1}^{(k-1)}, \mathbf{u}_{m-\mu_m+2}^{(k-1)}, \ldots, \mathbf{u}_m^{(k-1)}] \in C^{m \times \mu_m}$. $\mathbf{u}_{m-\mu_m+1}^{(k-1)}, \mathbf{u}_{m-\mu_m+2}^{(k-1)}, \ldots, \mathbf{u}_m^{(k-1)}$ are the eigenvectors of the smallest eigenvalue of $\mathbf{A}_{k-1}^H \mathbf{A}_{k-1}$ with multiplicity μ_m.

After getting the projection matrix in each iteration, the cost function (16) can be evaluated for the selection. The detailed CMPME operations are shown in Algorithm 1. In its implementation, the cost function evaluation causes the dominant computational cost. To determine the kth spatial sample position, it costs $O(m^2(N - k + 1)Q + mQ^2(N - k + 1))$. Therefore, the total complexity cost can be estimated as $O((m^2 + mQ)NQM)$.

B. Efficient Implementation

In Algorithm 1, two most computationally expensive steps are to evaluate the cost functions with respect to the observation vectors of each candidate sample (line 6 or 10 in the algorithm), and to compute and update the set of orthonormal bases (line 7 or 11). As the cost function of each candidate sample is evaluated with respect to the same set of orthonormal bases, it can be implemented by parallel computing.

For the update of the orthonormal bases and projection operator, the computation load can be significantly reduced by iterative computing. More specifically, the orthonormal bases $\mathbf{R}_{k-1}$ (in line 7) are computed through the orthonormalization of the column vectors of $\mathbf{A}_{k-1}^H$ and then expanded to $\mathbf{R}_k$ after appending new observation vectors $\mathbf{\Phi}_{\hat{s}_k}$ to $\mathbf{A}_{k-1}$, which can be expressed as $\mathbf{R}_k = \text{orth}(\mathbf{A}_k^H) = \text{orth}([\mathbf{A}_{k-1}^H \quad \mathbf{\Phi}_{\hat{s}_k}^*])$, and the superscript $*$ represents the complex conjugate. As in the previous iteration $\mathbf{R}_{k-1} = \text{orth}(\mathbf{A}_{k-1}^H)$ has been computed and orthonormal column vectors are obtained, $\mathbf{R}_k$ can be updated by only orthonormalizing $\mathbf{\Phi}_{\hat{s}_k}^*$ relative to $\mathbf{R}_{k-1}$ via Gram-Schmidt (G-

S) process. After obtaining $\mathbf{R}_k$, the projection operator $\mathbf{P}_k$ can also be updated. This update process can be expressed as

$$
\begin{aligned}
\mathbf{P}_k &= \mathbf{I}_{m \times m} - \mathbf{R}_k \mathbf{R}_k^H \\
&= \mathbf{I}_{m \times m} - \mathbf{R}_{k-1} \mathbf{R}_{k-1}^H \\
&\quad - \operatorname{orth}(\mathbf{\Phi}_{\hat{s}_k}^*; \mathbf{R}_{k-1}) \operatorname{orth}(\mathbf{\Phi}_{\hat{s}_k}^*; \mathbf{R}_{k-1})^H \\
&= \mathbf{P}_{k-1} - \operatorname{orth}(\mathbf{\Phi}_{\hat{s}_k}^*; \mathbf{R}_{k-1}) \operatorname{orth}(\mathbf{\Phi}_{\hat{s}_k}^*; \mathbf{R}_{k-1})^H. \quad (19)
\end{aligned}
$$

where $\operatorname{orth}(\mathbf{\Phi}_{\hat{s}_k}^*; \mathbf{R}_{k-1})$ denotes the new orthonormal bases of $\mathbf{\Phi}_{\hat{s}_k}^*$ relative to $\mathbf{R}_{k-1}$. So one can see that the cost function can be updated by just computing the projections of the observation vectors of the remaining sensors with respect to the second term in the last line of (19). As the column dimension of $\operatorname{orth}(\mathbf{\Phi}_{\hat{s}_k}^*; \mathbf{R}_{k-1})$ is much smaller than that of $\mathbf{R}_k$, i.e., $Q \ll m$, so the computational load for the cost function evaluation in line 6 is substantially reduced through sequential update in each iteration.

In line 11, the column vectors of $\mathbf{U}$ form a set of orthonormal bases, which is obtained through SVD: $\mathbf{A}_k^H = \mathbf{U}^{(k)} \mathbf{\Sigma}^{(k)} (\mathbf{V}^{(k)})^H$. As the dimensions of matrix $\mathbf{A}_k$ are typically of hundreds and thousands in the imaging case, the SVD of $\mathbf{A}_k^H$ is very computationally expensive. Considering the fact that $\mathbf{A}_k$ is obtained by appending a small matrix $\mathbf{\Phi}_{\hat{s}_k}$ to the row space of $\mathbf{A}_{k-1}$, then its SVD can be obtained by consecutively performing Q times rank-1 update to the SVD of $\mathbf{A}_{k-1}$ [28], [29]. Finally, we want to mention that these efficient implementation methods can also be used to accelerate the traditional MPME algorithm.

IV. IMAGING EXAMPLES

This section presents some examples to show the imaging performance of sensor arrays optimized with the proposed algorithm. For comparison purposes, the simulations were also carried out with the clustered FrameSense (CFS) method, CSBS [23] and the convex relaxed method [17]. The convex relaxed method was implemented with a MATLAB software for semidefinite-quadratic-linear programming, i.e., SDPT3 software package [30].

A. Planar Array Imaging

Firstly, a circular planar array based imaging is presented to demonstrate the performance of the four methods for antenna array topology optimization. Assume a circular planar array of radius 0.5 m was used for signal acquisition and it was located on the xoz plane. The y-axis pointed towards the illuminated region and formed a right-hand coordinate system with the x and z axes. The operational bandwidth was from 2 to 6 GHz. The scene of interest was a volume with the closest distance of 0.5 m from the array and its dimensions were 0.6 m × 0.2 m × 0.6 m in the $x, y,$ and z axes, respectively. So the cross-range and down-range resolution can be estimated as 2.25 cm and 3.75 cm. Considering the computational time for the simulation, we divided the scene of interest as the voxels with dimensions of 5 cm × 5 cm × 5 cm. So the whole imaging volume contains 845 voxels. In the circular antenna array, the candidate spatial samples of the antennas lie on a series of concentric circles with radii ranging from 0.05 m to 0.5 m with steps of 5 cm. In azimuth, the sampling interval was 6°. Therefore, we have 600 candidate spatial samples within the aperture in total. Moreover, at each spatial sampling position an antenna takes 41 measurements with the frequencies sweeping from 2 to 6 GHz with steps of 100 MHz.

In the simulation, for each measurement the following signal model was used

$$
s(\mathbf{x}_a, f) = \int_V \chi(\mathbf{x}) \cdot \frac{\exp(-j4\pi f R/c)}{4\pi R} \, \mathrm{d}V \quad (20)
$$

where $\mathbf{x}_a$ and $\mathbf{x}$ represent the antenna's and the scatterers' positions, respectively. c is the wave propagation speed, f is the signal frequency, $\chi(\cdot)$ is the reflectivity function and $R = |\mathbf{x} - \mathbf{x}_a|$ is the distance between the antenna and the scatterer. Note that in (20) a monostatic radar configuration is considered; thus the positions of each transmitter and receiver pair in (1) are simply denoted by the antenna position $\mathbf{x}^a$. The second term $\exp(-j4\pi f R/c)/4\pi R$ represents the round-trip wave propagation model.

Setting $\chi(\mathbf{x}) = 1$ and applying the spatial box window at each voxel in (20), the initial sensing matrix $\tilde{\mathbf{A}} \in C^{24600 \times 845}$ associated with all the candidate spatial samples can be constructed.

Based on the aforementioned simulation setup and signal model, the spatial samples for circular planar array were selected with CMPME, CFS, CSBS, and the convex relaxed method. Here as long as a spatial sampling position was selected, the observation vectors corresponding to all the 41 frequencies were chosen. Assume $\mathbf{n}$ is independent and identically distributed (i.i.d.) Gaussian noise, with the variance $\sigma^2 = 1$. Then the MSE, WCEV and condition numbers achieved by the observation matrices constructed with the observation vectors selected by the four methods are presented in Fig. 2.

From Fig. 2(a), it can be seen that the spatial samples selected with CMPME achieve smaller MSE, WCEV and condition numbers compared to the CFS. Moreover, with sufficient spatial samples (more than 60 spatial samples), the CMPME also leads to slightly better selection than the CSBS. However, when the number of selected spatial samples is small (less than 50), the CSBS performs slightly better than the CMPME. This is because CSBS is, similar to the CFS, a greedy 'worst-out' algorithm, which gradually removes the least informative spatial samples. Then the most informative ones are selected in terms of MSE. By contrast, the CMPME takes a sequential forward selection scheme. It gradually adds to the selection set the sample that is most complementary to the existing ones. So the spatial samples selected by CMPME could be less optimal than that selected by CSBS when the number of samples is small. Nevertheless, 50 spatial samples are not sufficient as the MSEs achieved by the observation matrices obtained with both methods are larger than 10^5. With the increase of the number of selected spatial samples, the CMPME and CSBS achieve equivalent performance in terms of MSE. Meanwhile, the CFS reaches the comparable but slightly larger MSE compared to CMPME and CSBS. This is due to the fact that in the simulation scenario the distances from different antenna positions to scatterers have very small differences. Namely, the observation vectors associated with different spatial samples have more or less similar norms, in which case the frame potential can lead
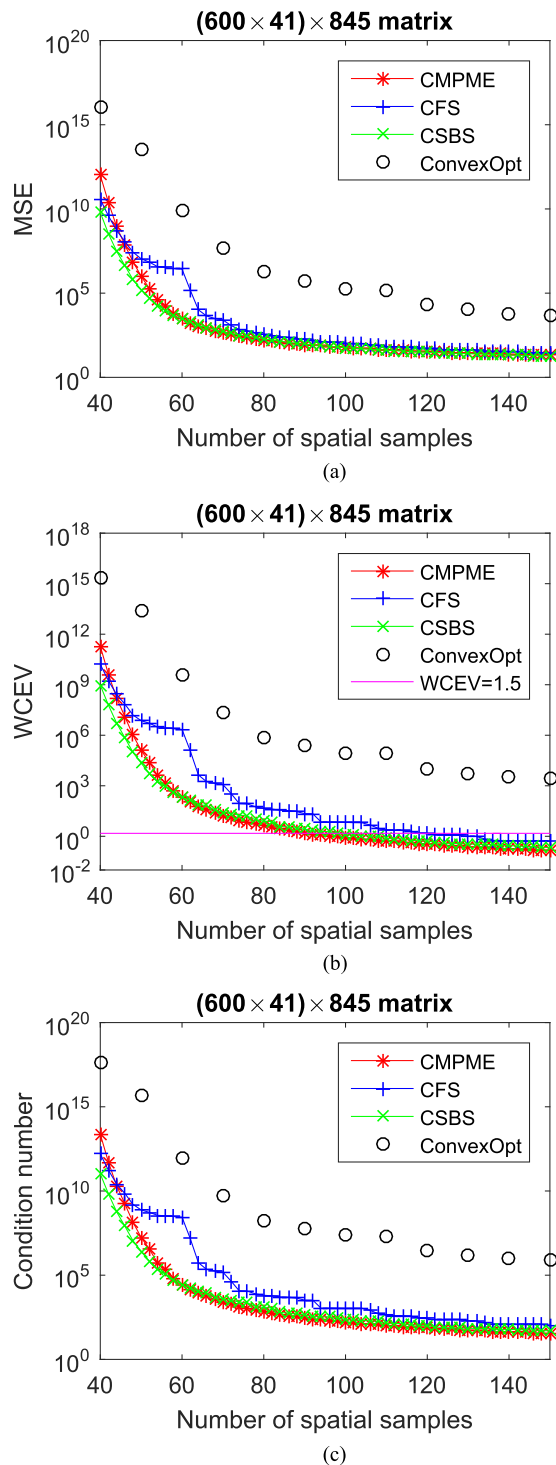
Fig. 2.   Criteria comparison of the three selection approaches. (a) Shows the MSEs achieved by the observation matrices with different number of selected spatial sampling positions; (b) for WCEV, and (c) for condition number.
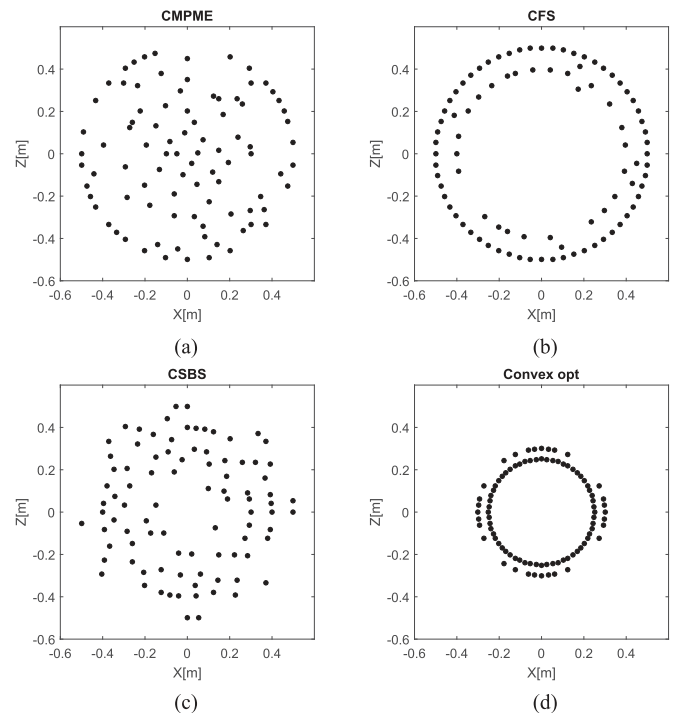

Fig. 3.   Array topologies of 90 selected spatial samples with (a) CMPME, (b) CFS, (c) CSBS, and (d) convex optimization.

and CFS outperform the convex relaxed method in this case in terms of MSE.

The variations of the WCEVs and condition numbers of the observation matrices obtained with the four methods are shown in Fig. 2(b) and (c). Similar to the MSE in Fig. 2(a), the WCEVs and condition numbers rapidly decrease with the growth of the number of spatial samples. Overall, CMPME and CSBS arrive at better performances than CFS and the convex relaxed method in terms of both WCEVs and the condition numbers. Moreover, with sufficient spatial samples, CMPME results in smaller WCEVs and condition numbers compared to CSBS. If we set the WCEV threshold as 1.5, the numbers of the spatial samples selected by CMPME, CSBS, and CFS are 90, 98 and 118, respectively. Meanwhile, the convex relaxed optimization method leads to more than 150 samples to be selected. Therefore, among the four methods, CMPME selects the minimum number of spatial samples.

To further compare the imaging performance of the arrays obtained with the four methods, we take arrays of 90 spatial samples as an example. The topologies of the circular arrays acquired with the four methods are shown in Fig. 3. Intuitively, the arrays selected with CMPME and CSBS have relatively uniform distributions of the spatial samples within the aperture while the samples of the array obtained with the CFS are mainly located on the circles close to the edge of the aperture. Although the spatial samples selected by the convex relaxed method are also mainly distributed on two circles, they form a smaller effective aperture compared to those acquired with the other three greedy algorithms. Therefore, it would result in, according to the array theory, lower cross-range resolution than that with the other three arrays.

to the optimal selection. Therefore, the CFS achieves comparable performance as CMPME and a similar phenomenon was also observed for FrameSense and MPME [19]. Furthermore, it is obvious that the observation matrices selected by CMPME, CSBS and CFS arrive at much smaller MSE than that obtained with the convex relaxed method. So all the CMPME, CSBS,
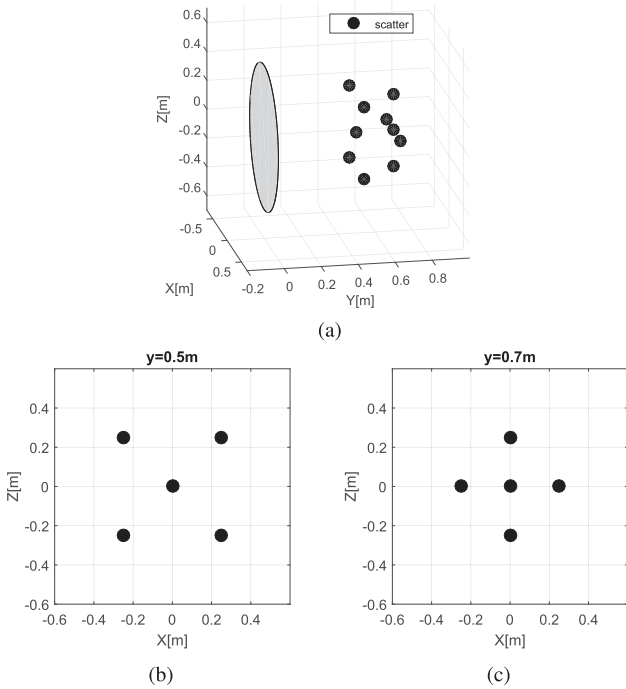
Fig. 4. Measurement setup for numerical simulations with the four arrays. (a) 3-D view of the imaging configuration, where the shaded circular area on $y = 0$ indicates the antenna aperture, (b) slice at $y = 0.5$ m, and (c) slice at $y = 0.7$ m.

Imaging simulations were performed for the four arrays with the measurement setup shown in Fig. 4. Ten point targets were placed on two planes $y = 0.5$ m and $y = 0.7$ m [see Fig. 4(b) and (c)] and the magnitudes of their reflectivity functions were set to two. The measurement errors and noise were assumed to be the zero-mean Gaussian distribution with the variance equal to one, i.e., $\mathbf{n} \sim \mathcal{N}(0, 1)$ (correspondingly, the signal to noise ratio ≤ 5.6 dB). Taking 50 Monte Carlo runs each with a different noise realization, the average of the imaging results on the two target planes are presented in Fig. 5 and Fig. 6 in the logarithmic scale. For comparison, the truths of the target setting at the two slices are also shown in Fig. 5(a) and Fig. 6(a), respectively. It is obvious that the arrays selected with CMPME, CFS, and CSBS result in much better estimations of the imaging scenes in contrast to the array acquired with the convex relaxed method. In the images estimated by the three greedy algorithms, some fluctuations are noticed in the "floor" region compared to their corresponding truths but the differences among them are hard to be distinguished visually. The quantitative metrics, i.e., MSE and WCEV, of the reconstructed 3-D images were examined and listed in Table I. One can see that the array selected by CMPME achieves the smallest MSE and WCEV for the estimated images while the array obtained with the convex relaxed method leads to the worst estimation of the image. As the WCEV = 1.5 (the solid line in Fig. 2(b)) was used as a threshold to determine the number of spatial samples (i.e., 90 samples), it is indeed achieved with the array designed by CMPME.

Although the variance of the noise was set to one in the above numerical simulation, it should be noted that the noise has no influence on the performance of the proposed CMPME selection

approach. CMPME selects the sensors/samples by assessing the contributions of their observation vectors to the minimum eigenspace of $\mathbf{A}^H \mathbf{A}$, where observation vectors are assumed to be known. The selected observation vectors gradually expand the row space or increase the minimum singular value(s) of the constructed observation matrix, thus reducing its condition number and improving the stability of the inversion. However, if the observation matrix constructed with the selected observation vectors still has very small singular values (equivalently, a large condition number), data errors caused by the noise would lead to much larger errors in the inversion results. In such circumstances, regularization methods should be used to suppress the effects of the noise on image reconstruction.

Finally, the computational complexities of the four algorithms are compared. As indicated in [17] and [19], the computational complexity of the convex relaxed method for selecting sensors with vector measurements is $O(i_c N^3 Q^3)$, where i_c is the iterative number of the convex optimization. Meanwhile, the computational cost of CSBS is given as $O(mN^3 Q^2)$[23]. For the CFS, $N - M$ spatial samples are removed one by one. The computational cost to remove the kth sensor is $O(2m[(N - k + 1)Q]^2)$. Therefore, the total computational cost can be expressed as $O(2m \sum_{k=1}^{N-M} [NQ - (k - 1)Q]^2) \approx O(\frac{2}{3}mQ^2(N^3 - M^3))$. If the matrix $\tilde{\mathbf{A}}\tilde{\mathbf{A}}^H$ can be stored, then the computational cost of CFS would be further reduced to $O(2mN^2 Q^2)$. For the convenience of comparison, the computational complexities of the four methods are summarized in Table II where $\tilde{L} = N \cdot Q$ is used to simplify the notation. As typically $\tilde{L} \gg m, N, Q$, so one can see among the four algorithms CMPME has the lowest computational complexity followed by CFS. This results from the fact that the CMPME is a sequential forward selection approach instead of the sequential backward selection schemes used in CSBS and CFS. This advantage could be even remarkable when the number of selected samples is substantially smaller than that of the candidate samples. For the planar array imaging simulations above, the computational time of the four algorithms also proves this conclusion, as shown in Table III. In this simulation, the sensor selection simulations were performed on a PC with an Intel Core i5-3470 CPU of 3.2 GHz and 8 GB RAM. All the four methods were implemented in Matlab code. For the convex relaxed method, 21 iterations were automatically performed by SDPT3 optimization engine. From Table III, one can see that in this simulation CFS and CMPME are more than 100 times faster than the convex relaxed method and CSBS. Moreover, the circular array selected by CMPME achieves the comparable imaging performance as that obtained by CSBS.

B. Optimization of 3-D Synthetic Array

In this section, we present the sampling design and optimization of a 3-D array (i.e., E-RadSAR) for 3-D imaging by using the proposed algorithm.

A 3-D GPR imaging simulation was performed for illustration of the proposed algorithm for the E-RadSAR sampling design. The simulation configuration is shown in Fig. 7. Two perpendicularly oriented dielectric cylinders were buried in the soil
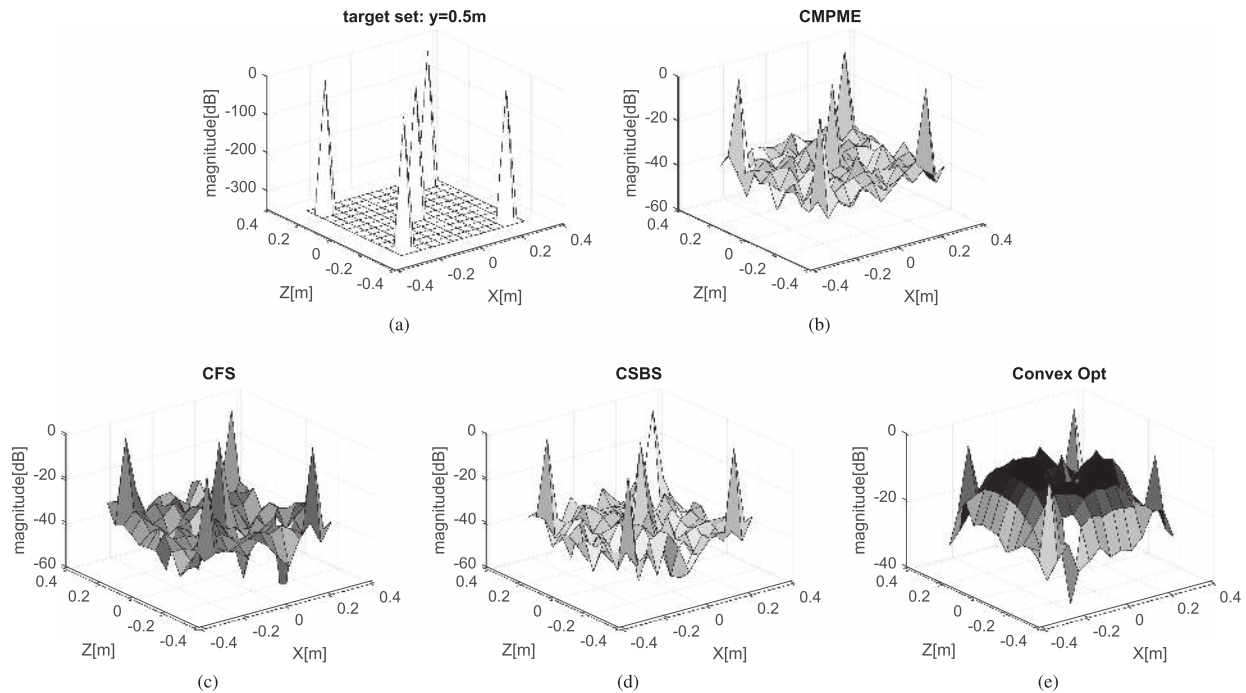
Fig. 5.   Comparison of imaging results at the slice $y = 0.5$ m obtained with the arrays optimized by four different approaches. (a) Shows the truth of the target configuration, (b)–(e) are the slice images obtained with the arrays selected by CMPME, CFS, CSBS, and convex relaxed optimization method, respectively.
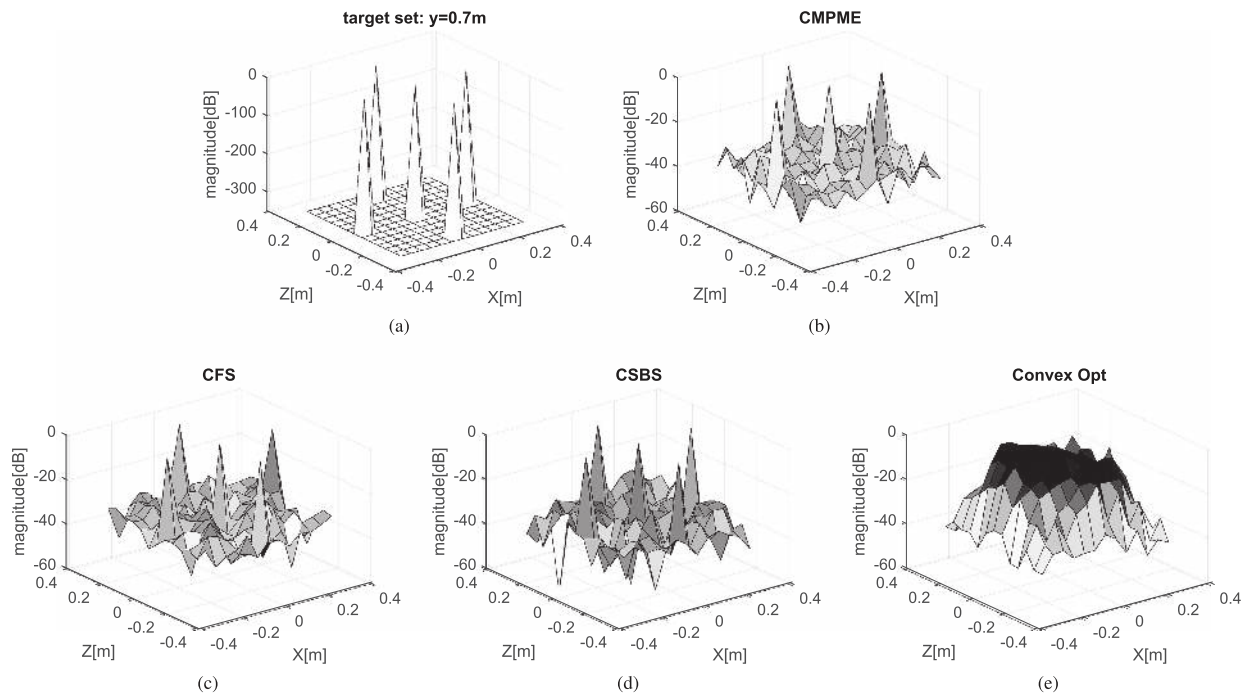

Fig. 6.   Comparison of imaging results at the slice $y = 0.7$ m obtained with the arrays optimized by four different approaches. (a) Shows the truth of the target configuration, (b)–(e) are the slice images obtained with the arrays selected by CMPME, CFS, CSBS, and convex relaxed optimization method, respectively.

as the objects and they were joined at one end. The radius of the cylinders is 10 cm and their lengths are 60 cm and 80 cm. The conductivity and relative permittivity of the cylinders are 0.05 S/m and 5.0, respectively. In addition, the permittivity of the background soil is 9.0 and its conductivity 0.01 S/m. The elementary dipole antennas were placed along a radius of a circle centered at the origin on the ground surface (i.e., xoz-plane

in Fig. 7). The orientations (i.e., polarizations) of the dipole antennas were also along the radius. The Ricker wavelet with a center frequency of 900 MHz was used as the excitation signal. To simulate the operation of the GPR system used in the TBM, the GPR signals were acquired over several concentric circles with the rotation of the antennas around the origin. To get properly focused images of targets at a distance of 0.4 m,

TABLE I
MSEs AND WCEVs OF THE ESTIMATED IMAGES WITH THE ARRAYS
OPTIMIZED BY THE FOUR ALGORITHMS

Algorithms	CMPME	CFS	CSBS	ConvexOpt
MSE	88.96	185.11	96.06	5.08e+05
WCEV	0.88	2.41	0.96	1.24e+04

TABLE II
COMPUTATIONAL COMPLEXITIES OF THE FOUR ALGORITHMS

ConvexOpt	CSBS	CFS	CMPME
$O(i_c\tilde{L}^3)$	$O(mN\tilde{L}^2)$	$O(2m\tilde{L}^2)$	$O((m^2 + mQ)M\tilde{L})$

TABLE III
COMPUTATION TIME OF CMPME, CSBS, CFS, AND THE CONVEX RELAXED
METHOD TO SELECT 90 SPATIAL SAMPLES FROM 600 CANDIDATES FOR
PLANAR CIRCULAR ARRAY OPTIMIZATION

Algorithm	ConvexOpt*	CSBS	CFS	CMPME
Time	4.14h	3.92h	126.4s	91.8s

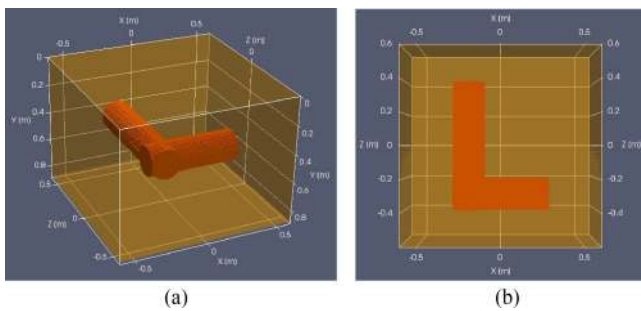* 21 iterations were taken.

Fig. 7. Geometrical configuration of GPR numerical simulation. (a) Is the 3-D illustration of the simulation setup, and (b) is its xoz-view along the y axis.

a circular planar array aperture of the radius 0.5 m should be used. Based on the polar sampling criteria, eight antennas were placed along a radial direction on eight concentric circles with the radius ranging from 0.15 m to 0.5 m with steps of 5 cm. In azimuth, the signals were measured every $3°$. Therefore, in total 960 spatial samples were acquired over the circular planar array.

To explore the possibility to reduce the number of antennas by taking advantage of the forward motion for 3-D array synthesize, three different depths of the objects, i.e., 0.3 m, 0.4 m, and 0.5 m, relative to the ground surface (i.e., antenna array) were considered to simulate the E-RadSAR. Taking the aforementioned sampling criteria, 2880 spatial samples were acquired over three planar circular arrays at the three depths, which form the candidate set for the E-RadSAR sampling design and optimization.

For convenience of description, let us set $y = 0$ at the closest position, i.e., 0.3 m in depth, of the antenna array relative to the objects. The imaging volume is a cuboid defined by $[-0.4, 0.4]$m $\times$ $[0.1, 0.5)$m $\times$ $[-0.5, 0.5]$m along the x, y and z directions. The whole volume is partitioned into 41820 voxel cells of the dimensions 2 cm $\times$ 2 cm $\times$ 2 cm in which the

values of voxels represent the reflectivity functions at the corresponding positions. Then the observation vectors of the antenna at each position at different signal frequencies relative to the imaging volume can be obtained via half-space Green's functions for the scattering process based on the Born approximation [31]. The signal frequencies sweep from 557.8 MHz to 1546.6 MHz with steps of 12.7 MHz to cover the effective bandwidth of the Ricker wavelet. So considering different frequencies, 79 observation vectors are obtained at each sampling position. Stacking all the observation vectors associated with all the candidate sampling positions at all the discrete frequencies, a candidate sensing matrix $\tilde{\mathbf{A}} \in C^{(2880·79)\times41820}$ is obtained. The candidate sensing matrix corresponds to the volume array synthesized by using eight antennas, and each antenna contributes 28440 (i.e., $120 \times 3 \times 79$) candidate observation vectors.

To design and optimize the sampling strategy of the 3-D synthetic array, we take two steps: the first step is to select a certain number of antennas from eight candidate antennas; the second step is to optimize the spatial sampling positions of the selected antennas. Considering the number of voxel cells in the imaging volume and slight redundancy for signal acquisition, at least three antennas should be selected. That is to say, at least three sub-matrices of the dimensions 28440×41820 should be chosen. Accounting for the enormous size of the candidate sensing matrix $\tilde{\mathbf{A}}$ and computational time, the first step was implemented by using CFS [24]. The outer-most three antennas within the circular aperture were selected, as shown in Fig. 8(a).

Next, the spatial sampling positions of the three selected antennas are selected. Considering both the selection performance and the computational time, CMPME and CFS were used to select the (near-)optimal spatial samples, and the imaging performances of their selected arrays were compared. In this example, 350 spatial sampling positions were selected for the three antennas. The selected results are shown in Fig. 8(b) and (c). Comparing Fig. 8(b) and (c), one can see that the CFS selects mainly the spatial samples that are far from the imaging volume while CMPME selects the nearer ones. This can be explained as follows. CFS gradually eliminates the spatial samples whose observation vectors have the largest frame potential (i.e., correlations) with those of the rest samples, which works optimally for observation vectors with equal ℓ_2 norms. But for observation vectors with unequal norms, the performance of CFS is degraded. Considering attenuation and spread loss of wave propagation, the observation vectors at the spatial sampling positions closer to the imaging volume have larger ℓ_2 norms than those at a longer distance. So when evaluating the frame potential via inner product, the observation vectors with larger ℓ_2 norms could lead to larger frame potentials. Thus, the corresponding spatial samples, i.e., those at short range, are discarded, which has also been indicated for the traditional FrameSense method [16]. By contrast, CMPME evaluates the complementary information introduced by the observation vectors associated with a new spatial sample relative to the existing ones, which takes into account the effects of the magnitudes of the observation vectors. The spatial sampling positions at a shorter distance form relatively diverse observation angles with respect to the imaging volume and their observation vectors have larger magnitudes,
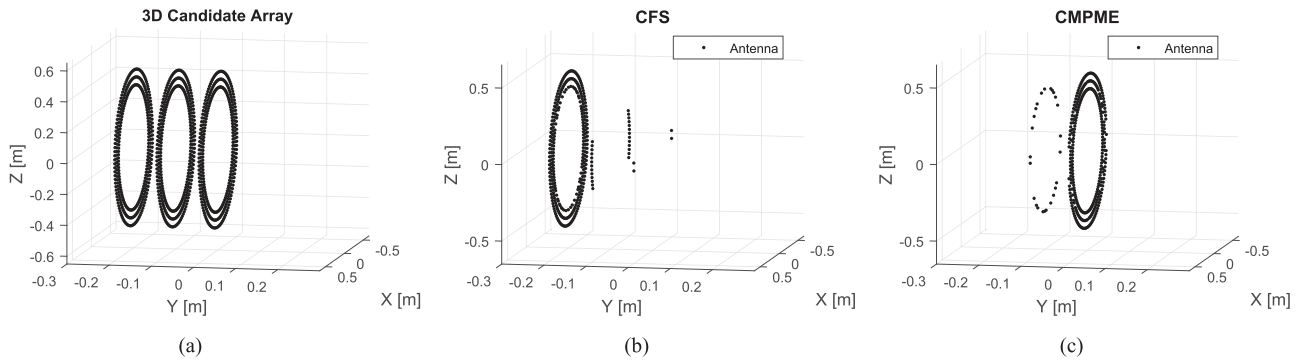
Fig. 8. Spatial sample selection for 3-D synthetic array. (a) Shows the candidate spatial samples of the selected antennas; (b) and (c) show the 350 spatial samples selected for the three antennas with CFS and CMPME, respectively.
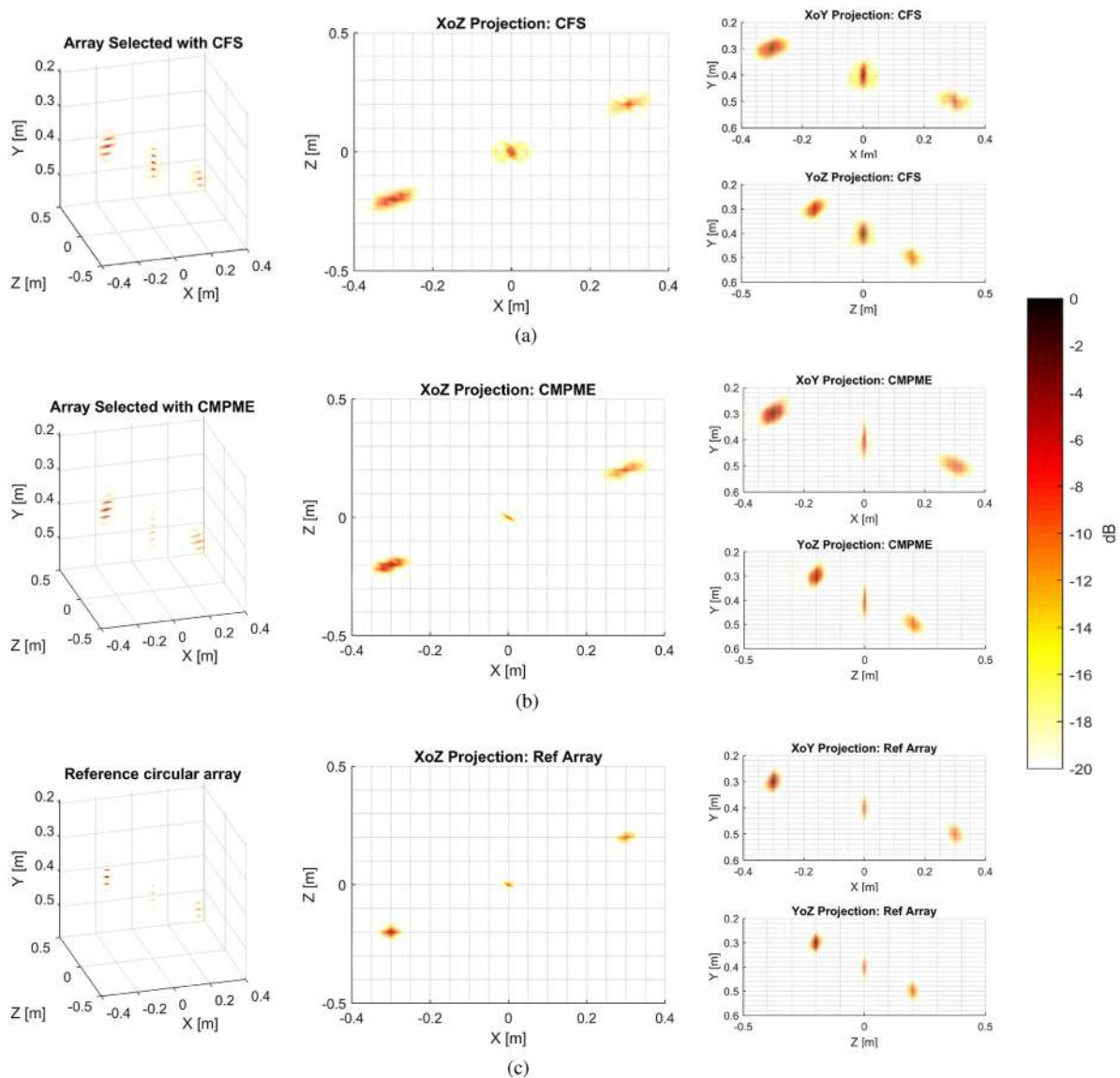

Fig. 9. Point spread functions of the 3-D arrays selected with CFS and CMPME as well as a reference circular array. (a) Shows the 3-D point spread functions of the 3D array selected with CFS at $(-0.3, 0.3, -0.2)$ m, $(0, 0.4, 0)$ m, and $(0.3, 0.5, 0.2)$ m and their projections on the xoy, yoz, and zox planes; (b) the related point spread functions of the 3-D array selected with CMPME and their projections on three planes; and (c) the point spread functions and three projections of a RadSAR which is synthesized at $y = 0$ by using all eight candidate antennas and acquires 960 spatial samples.

thus resulting in large projections onto the minimum eigenspace. Consequently, the spatial samples closer to the imaging volume are preferably selected by CMPME algorithm.

To show the imaging performance of the 3-D arrays selected with the two methods, their point spread functions (PSF) are firstly evaluated at three positions, i.e., $(-0.3, 0.3, -0.2)$ m, $(0, 0.4, 0)$ m, and $(0.3, 0.5, 0.2)$ m within the imaging volume and the obtained 3-D PSFs and their 2-D projections on the xoy-, yoz- and zox-planes are presented in Fig. 9(a) and (b). One can see both 3-D arrays provide well-focused PSFs. However, the 3-D array selected with CMPME achieves better cross-range resolution than that of the 3-D array obtained with CFS, which can be obviously observed from the PSFs at $(0, 0.4, 0)$ m. This is due to the fact that the 3-D array selected by CMPME contains more spatial samples (i.e., the ones at $y = 0$) closer to the imaging volume and forms a broad range of observation aspects relative to objects, thus resulting in higher cross-range resolution compared to that selected with CFS. In terms of the down-range resolution, both arrays perform comparably as the signal bandwidths, which play a major role in determining the down-range resolution, are equal. In addition, for comparison, Fig. 9(c) shows the corresponding PSFs of a RadSAR synthesized by all eight candidate antennas on the plane $y = 0$ which took 960 spatial samples within the aperture. Comparing Fig. 9(a) and (b) with (c), some degradation of spatial resolutions, especially the cross-range resolutions of the 3-D E-RadSAR arrays selected with CFS and CMPME, is observed compared to that of the RadSAR. However, this loss in spatial resolution is very tinny or acceptable in contrast to the reduction of almost two-thirds of antennas and spatial samples needed for signal acquisition. So E-RadSAR provides an effective approach to reduce antennas needed by the traditional RadSAR.

The 3-D images of the extended cylindrical objects mentioned above were also reconstructed to further demonstrate the imaging performance of the 3-D E-RadSAR arrays selected with the two methods and the focused images are shown in Fig. 10. One can see that the images of the cylinders are well reconstructed with both 3-D arrays [Fig. 10(a) and (c)]. From the top-views of the 3-D images [Fig. 10(b) and (d)], it can be observed that the artifacts in the image obtained with the 3-D array selected with CMPME are considerably suppressed compared to that in the image with the array selected with CFS. So in terms of the overall image quality, the 3-D array selected with CMPME outperforms that obtained with CFS. Moreover, some other differences are also noticed in the focused images with the two 3-D arrays. From Fig. 10(d), it seems that the focused images of the cylinders are slightly distorted, i.e., curved. This is because the antennas in the array selected with CMPME form relatively large observation angles from the broadside of the antennas. Then due to the weighting effects of the antenna radiation pattern, reflected signals from some scatterers are not well acquired or even missing. Thus it causes slight distortion in the focused images.

Here we have to mention that 350 spatial samples selected in this example lead to an observation matrix $\mathbf{A} \in \mathbb{C}^{27650 \times 41820}$ whose rank is still smaller than the number of voxel cells. This could also be a reason for the distortion of the focused image
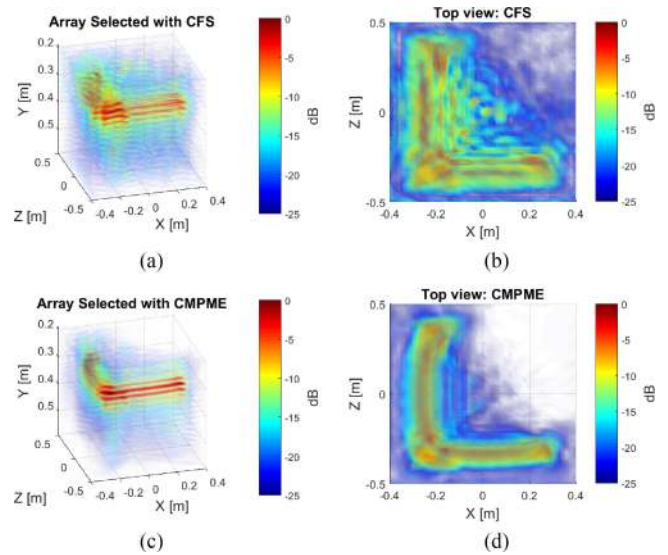

Fig. 10. Imaging results of the selected 3-D synthetic arrays with CFS and CMPME algorithms. (a) and (c) are the reconstructed 3-D images with the 3-D arrays selected by CFS and CMPME; (b) and (d) display their top-views, respectively.

with the array selected with CMPME. By increasing the number of selected spatial samples, the imaging performance of the 3-D array obtained with CMPME could be further improved.

V. CONCLUSION

In this paper, the clustered MPME approach has been developed to select sensors/spatial samples with vector measurements so as to get a near-optimal observation matrix for microwave imaging. As the CMPME selects a group of observation vectors related to the same sensor at a time, the selection criterion evaluates not only the projection of each group of candidate observation vectors onto the minimum eigenspace related to the subspace spanned by the existing observation vectors but also their "orthogonality" among elements within each group compared to the MPME.

The analyses of the computational complexity and the selection performance reveal that the CMPME is not only one of the most efficient algorithms but also achieves the near-optimal selection in terms of both MSE and WCEV of the reconstructed images in contrast to the state of the art. Moreover, as a forward greedy algorithm, CMPME gradually expands the subspace spanned by the observation vectors. It guarantees the constructed observation matrix to be well conditioned, which is inherited from the MPME. These have been demonstrated through a planar imaging array design and an E-RadSAR sampling design. Furthermore, we have to mention that CMPME is a generic selection algorithm and applicable to general linearized measurement scheme for imaging systems. In the paper, it has been applied to the Born-based linear inversion, but the approach itself is not limited to the area of applicability of the Born approximation itself. For more complicated non-linear imaging/inversion formulations, the related sensor selection problem should be further studied in future.

REFERENCES

[1] M. Soumekh, *Synthetic Aperture Radar Signal Processing With MATLAB Algorithms*. New York, NY, USA: Wiley, 1999.

[2] Z. Li, J. Wang, J. Wu, and Q. H. Liu, "A fast radial scanned near-field 3-D SAR imaging system and the reconstruction method," *IEEE Trans. Geosci. Remote Sens.*, vol. 53, no. 3, pp. 1355–1363, Mar. 2015.

[3] J. Wang, P. Aubry, and A. Yarovoy, "A novel approach to full-polarimetric short-range imaging with copolarized data," *IEEE Trans. Antennas Propag.*, vol. 64, no. 11, pp. 4733–4744, Nov. 2016.

[4] J. Wang, H. Cetinkaya, and A. G. Yarovoy, "Comparison of CSAR, E-CSAR and planar circular array for 3-D imaging," in *Proc. IET Int. Radar Conf.*, Oct. 2015, pp. 1–5.

[5] W. Yao, D. N. Stephens, and M. O'Donnell, "Optimizing the beam pattern of a forward-viewing ring-annular ultrasound array for intravascular imaging," *IEEE Trans. Ultrason., Ferroelect., Freq. Control*, vol. 49, no. 12, pp. 1652–1664, Dec. 2002.

[6] J. Wang, H. Cetinkaya, A. Yarovoy, I. I. Vermesan, and S. Reynaud, "Investigation of forward-looking synthetic circular array for subsurface imaging in tunnel boring machine application," in *Proc. 8th Int. Workshop Adv. Ground Penetrating Radar*, 2015, pp. 1–4.

[7] B. Steinberg and H. Subbaram, *Microwave Imaging Techniques* (Wiley Series in Remote Sensing and Image Processing). New York, NY, USA: Wiley, 1991.

[8] O. M. Bucci and G. Franceschetti, "On the degrees of freedom of scattered fields," *IEEE Trans. Antennas Propag.*, vol. 37, no. 7, pp. 918–926, Jul. 1989.

[9] F. Soldovieri, R. Solimene, and F. Ahmad, "Sparse tomographic inverse scattering approach for through-the-wall radar imaging," *IEEE Trans. Instrum. Meas.*, vol. 61, no. 12, pp. 3340–3350, Dec. 2012.

[10] R. Solimene, M. A. Maisto, G. Romeo, and R. Pierri, "On the singular spectrum of the radiation operator for multiple and extended observation domains," *Int. J. Antennas Propag.*, vol. 2013, 2013, Art. no. 585238.

[11] J. L. Schwartz and B. D. Steinberg, "Ultrasparse, ultrawideband arrays," *IEEE Trans. Ultrason., Ferroelect. Freq. Control*, vol. 45, no. 2, pp. 376–393, Mar. 1998.

[12] Y. Gao and S. J. Reeves, "Optimal k-space sampling in MRSI for images with a limited region of support," *IEEE Trans. Med. Imag.*, vol. 19, no. 12, pp. 1168–1178, Dec. 2000.

[13] S. J. Reeves and L. P. Heck, "Selection of observations in signal reconstruction," *IEEE Trans. Signal Process.*, vol. 43, no. 3, pp. 788–791, Mar. 1995.

[14] S. J. Reeves and Z. Zhao, "Sequential algorithms for observation selection," *IEEE Trans. Signal Process.*, vol. 47, no. 1, pp. 123–132, Jan. 1999.

[15] R. Broughton, I. Coope, P. Renaud, and R. Tappenden, "Determinant and exchange algorithms for observation subset selection," *IEEE Trans. ImageProcess.*, vol. 19, no. 9, pp. 2437–2443, Sep. 2010.

[16] J. Ranieri, A. Chebira, and M. Vetterli, "Near-optimal sensor placement for linear inverse problems," *IEEE Trans. Signal Process.*, vol. 62, no. 5, pp. 1135–1146, Mar. 2014.

[17] S. Joshi and S. Boyd, "Sensor selection via convex optimization," *IEEE Trans. Signal Process.*, vol. 57, no. 2, pp. 451–462, Feb. 2009.

[18] S. P. Chepuri and G. Leus, "Sparsity-promoting sensor selection for nonlinear measurement models," *IEEE Trans. Signal Process.*, vol. 63, no. 3, pp. 684–698, Feb. 2015.

[19] C. Jiang, Y. Soh, and H. Li, "Sensor placement by maximal projection on minimum eigenspace for linear inverse problems," *IEEE Trans. Signal Process.*, vol. 64, no. 21, pp. 5595–5610, Nov. 2016.

[20] C. Rusu, J. Thompson, and N. M. Robertson, "Sensor management with time, energy and communication constraints," *IEEE Trans. Signal Process.*, vol. 66, no. 2, pp. 528–539, Jan. 2017. [Online]. Available: http://arxiv.org/abs/1702.04927

[21] M. Shamaiah, S. Banerjee, and H. Vikalo, "Greedy sensor selection: Leveraging submodularity," in *Proc. 49th IEEE Conf. Decis. Control*, Dec. 2010, pp. 2572–2577.

[22] I. Ivashko, G. Leus, and A. Yarovoy, "Radar network topology optimization for joint target position and velocity estimation," *Signal Process.*, vol. 130, pp. 279–288, 2017.

[23] B. Sharif and F. Kamalabadi, "Optimal sensor array configuration in remote image formation," *IEEE Trans. Image Process.*, vol. 17, no. 2, pp. 155–166, Feb. 2008.

[24] J. Wang and A. Yarovoy, "Near-optimal selection of GPR observations for linear inversion," in *Proc. 9th Int. Workshop Adv. Ground Penetrating Radar*, 2017, pp. 1–5.

[25] C.-T. Yu and P. K. Varshney, "Sampling design for Gaussian detection problems," *IEEE Trans. Signal Process.*, vol. 45, no. 9, pp. 2328–2337, Sep. 1997.

[26] J. Kruk, C. Wapenaar, J. Fokkema, and P. van den Berg, "Three-dimensional imaging of multicomponent ground penetrating radar data," *Geophysics*, vol. 68, no. 4, pp. 1241–1254, 2003. [Online]. Available: http://library.seg.org/doi/abs/10.1190/1.1598116

[27] G. Golub and C. Van Loan, *Matrix Computations*. Baltimore, MD, USA: The Johns Hopkins Univ. Press, 1996.

[28] M. Brand, "Fast low-rank modifications of the thin singular value decomposition," *Linear Algebra Appl.*, vol. 415, no. 1, pp. 20–30, 2006.

[29] P. Stange, "On the efficient update of the singular value decomposition," *Proc. Appl. Math. Mech.*, vol. 8, no. 1, pp. 10827–10828, 2008. [Online]. Available: http://dx.doi.org/10.1002/pamm.200810827

[30] K. C. Toh, M. J. Todd, and R. H. Ttnc, "SDPT3 – A Matlab software package for semidefinite programming, version 1.3," *Optim. Methods Softw.*, vol. 11, no. 1–4, pp. 545–581, 1999.

[31] J. Wang, P. Aubry, and A. Yarovoy, "Efficient implementation of GPR data inversion in case of spatially varying antenna polarizations," *IEEE Trans. Geosci. Remote Sens.*, vol. 56, no. 4, pp. 2387–2396, Apr. 2018.
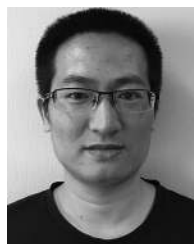
Jianping Wang received the B.Sc. degree from North China University of Technology, Beijing, China, in 2009, the M.Sc. degree from Beijing Institute of Technology, Beijing, China, in 2012, and the Ph.D. degree from Delft University of Technology, Delft, The Netherlands, in 2018, all in electrical engineering.

From August 2012 to April 2013, he was a Research Associate on FMCW SAR signal processing for formation flying satellites with the University of New South Wales, Sydney, NSW, Australia. He is currently a Postdoc Researcher with the group of Microwave Sensing, Signals and Systems, Delft University of Technology. His research interests include microwave imaging, signal processing, and antenna array design.

Alexander Yarovoy (F'15) received the Diploma (with honor) in radiophysics and electronics in 1984, and the Candidate Physics & Mathematics Science and Doctor Physics and Mathematics Science degrees in radiophysics in 1987 and 1994, respectively, all from the Kharkov State University, Kharkov, Ukraine.

In 1987, he as a Researcher joined the Department of Radiophysics, Kharkov State University, where he became a Professor in 1997. From September 1994 to 1996, he was a Visiting Researcher with the Technical University of Ilmenau, Ilmenau, Germany. Since 1999, he has been with the Delft University of Technology, Delft, The Netherlands, where since 2009, he has been leading as the Chair of Microwave Sensing, Signals and Systems. His main research interests include ultrawideband microwave technology and its applications (particularly radars) and applied electromagnetics (particularly UWB antennas). He has authored and coauthored more than 250 scientific or technical papers, 4 patents, and 14 book chapters.

Prof. Yarovoy was a Guest Editor for five special issues of the IEEE transactions and other journals. Since 2011, he has been an Associated Editor for the *International Journal of Microwave and Wireless Technologies*. He is the recipient of the European Microwave Week Radar Award for the paper that best advances the state of the art in radar technology in 2001 (together with L. P. Ligthart and P. van Genderen) and in 2012 (together with T. Savelyev). In 2010, together with D. Caratelli, he got the best paper award of the Applied Computational Electromagnetic Society. He was the Chair and TPC Chair for the 5th European Radar Conference (EuRAD 08), Amsterdam, The Netherlands, as well as the Secretary of the 1st European Radar Conference (EuRAD 04), Amsterdam. He was also the Cochair and TPC Chair of the 10th International Conference on Ground Penetrating Radar (GPR 2004) in Delft. Since 2008, he has been the Director of the European Microwave Association.